water

MDPI

Article

Study of Single Fracture Seepage Characteristics of Fault-Filled Materials Based on CT Technology

Wenbin Sun [1,2,3,*], Shaoyu Wang [1], Faxu Dong [1] and Yandong Xue [1]

[1] School of Energy and Mining Engineering, Shandong University of Science and Technology, Qingdao 266590, China
[2] State Key Laboratory of Coal Mining and Clean Utilization, Beijing 100013, China
[3] College of Earth and Mineral Sciences, The Pennsylvania State University, State College, PA 16801, USA
* Correspondence: swb@sdust.edu.cn

Abstract: In order to study the matrix loss process and skeleton seepage law in the fracture of the fault rock, the three-dimensional model of the skeletal rock sample of the fault rock was obtained by CT scan, and the porous media seepage model was established with different structural types of natural fractures, and the flow rate and pressure distribution law of the seepage in the fracture was obtained by FLUENT software simulation. The results show that: the seepage under different pressure conditions is approximately the same, and the velocity increases continuously with the increase in pressure; The water seepage in different directions of the fracture channels under the same pressure conditions is not exactly the same, which is caused by the different microstructures of the pores. For the pressure distribution, it gradually decreases along the direction of water seepage, and for the speed distribution, it shows the law of changing from large to small and then increasing.

Keywords: fissure; seepage; three-dimensional reconstruction; porous media; numerical simulation

Citation: Sun, W.; Wang, S.; Dong, F.; Xue, Y. Study of Single Fracture Seepage Characteristics of Fault-Filled Materials Based on CT Technology. *Water* **2022**, *14*, 3679. https://doi.org/10.3390/w14223679

Academic Editor: Jiutan Liu

Received: 26 October 2022
Accepted: 8 November 2022
Published: 14 November 2022

1. Introduction

With the gradual increase in the depth of coal mining in China, the safety risks faced are also increasing, and coal mine permeability accidents are still an important part of the accidents affecting coal mine production safety [1–5] and the economic losses caused by coal mine permeability have been the top of coal mine disasters. The fault is a weak geological structure that affects the safety of coal mining, and it is easy to form a water inrush channel in which the pressurized water of the aquifer layer conducts to the working face. Fault structure fill often consists of fault mud as a matrix and fault rock as the skeleton. The substrate in fault rock is very vulnerable to latent intrusion to form seepage channels [6,7], and under the support of the skeleton, the seepage channels expand to form a pipe surge through the fault, and the fault waterproof coal column is improperly retained or structural damage, and other protective measures fail, which will form water damage. Fault sudden water in coal mines [8–11] has gradually become a key scientific and technical problem that restricts the economic development of coal in China. From the case of sudden water of coal mine fault in past years, the sudden water of fault is influenced by the nature of its filling medium, especially the structure and permeability of the filling medium, so the study of the seepage characteristics of the fault filler is of great significance for the prediction of sudden water and its prevention and control.

Along with the rapid development of science and technology, computed tomography (CT) technology, three-dimensional microscopic imaging technology, focused ion beam-scanning electron microscopy (FIB-SEM), and magnetic resonance imaging (MRI) technology have become popular and widely used [12–17]. With the help of 3D digital core technology, porous media can be scanned from the nanometer to the micrometer level, enabling the reproduction of the real porous media pore structure with high accuracy, facilitating the observation of the degree of inhomogeneous changes in the internal structure

of pores, visualizing the internal structure of pores and achieving fine characterization, which will help to promote the progress of 3D structure measurement and characterization of porous media [18–23]. Wang Gang [24,25] established a 3D coal skeleton structure model containing pore fissures by using CT scanning and 3D reconstruction techniques, and the simulations demonstrated that a velocity peak and a stable flow rate value exist at each point in the pore fissures during seepage. Yao Banghua [26] established a multi-field coupled deformation-seepage erosion mechanics model for trapped column sudden water deformation based on dual pore medium seepage theory. Li Liping [27] used a computational procedure that can consider the dual damage criterion of rock tension shear and compression shear under the action of groundwater to reproduce the catastrophic evolution process of mining fracture sprouting, expansion, and penetration until rupture channel formation in the water-isolated rock body between the pressurized aquifer and the roadway.

Therefore, this paper explores the influence of the fracture structure of the original rock on the seepage law through the numerical simulation of the actual rock single fracture model. Combined with CT scanning and 3D reconstruction technology, a three-dimensional rock skeleton structure model containing pore fractures was established. On this basis, a porous medium model is constructed, and the flow velocity and pressure distribution of different seepage paths are obtained by simulating the seepage of a single fracture structure to explore the effects of different seepage paths and pressure and other factors on the seepage characteristics.

2. CT Scan and 3D Model Reconstruction

2.1. Pre-Processing of CT Scan Images

In this paper, the skeleton rocks of small fault filling collected during the roadway development in the Jining mining area of Shandong Province (the location is shown in Figure 1) were selected and made as dynamic metamorphic schist samples with a size of $7 \times 7 \times 30$ mm. The terrain in the mining area is undulating. The terrain is high in the south and low in the north, high in the west and low in the east, and high in the southwest and low in the northeast. The ground elevation is between 506.2~229.3 m, the relative height difference is 276.9m, and the average slope is about 3°46′. The CT scanning device nanoVoxel-3502E cross-scale core scanning imaging system is used to import the raw data file obtained by the CT scanning device into the AVIZO software. The CT scan reconstructs a model size of $600 \times 600 \times 1400$ voxels with 0.02381770 mm opaque voxel units and scans to obtain a 3D image of the rock sample. A 3D digital core model is constructed by region selection, sequence adjustment, angle correction, and black spot elimination of image slices. In order to extract the pore structure information from the scanned images, it is necessary to first separate the pore structure from the matrix skeleton, mainly using image filtering and threshold segmentation binarization techniques. After the core has been scanned, isolated pixel points with different grey scale values will appear due to interference from noise, etc. Noise is generally excluded by means of an islanding algorithm. For skeletons and pores, even the same rock components may show different greyscale values due to subtle differences in the nature of the mineral grains and their degree of metamorphism; Therefore, it is necessary to adopt appropriate filtering algorithms to remove noise interference and at the same time make the gray value distribution of the same component more concentrated, and the gray value distinction of different components more obvious, highlighting the pore fracture structure surface characteristics of rock samples, which is convenient for later threshold segmentation.

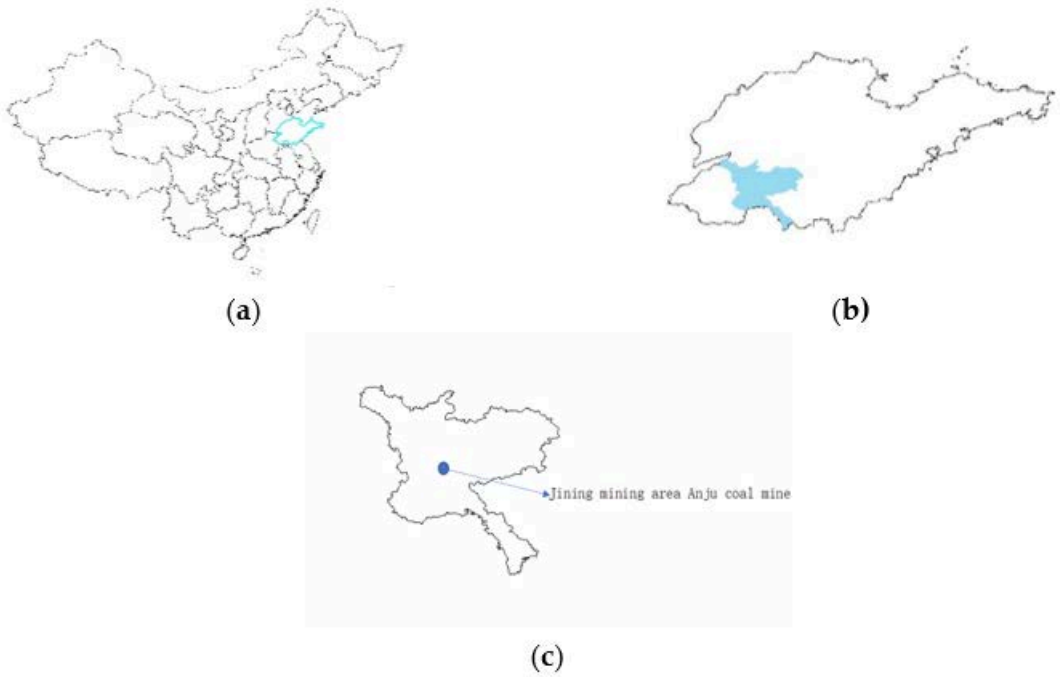

Figure 1. Mine Location Map: (**a**) Map of China. (**b**) Map of Shandong. (**c**) Diagram of Anju Coal Mine in Jining Mining District.

2.2. Fracture Extraction

The CT images are image processed, and 3D reconstructed to obtain a 3D pore model. After processing the model with Median Filtering and the threshold splitting binarization method, the appropriate fissure extraction was selected in the cropped model by AVIZO software (as shown in Figure 2). The cropped section is 150 × 150 × 150 voxels in size, and the sample contains a full fissure. After extracting the fissures, the surface of the fissures is smoothed, the entrance and exit of the fissures and the boundary conditions are set, the intersections are repaired, the number of faces is simplified so as to improve the quality of the mesh, and finally, a triangular mesh is generated on the surface of the fissures. After the meshing is completed, the quality of the mesh is checked, and low-quality, unconnected meshes are removed to ensure that a high-quality mesh is generated and finally saved as a cas format file, which is then imported into FLUENT software for the next numerical simulation.

3. Seepage Simulation

3.1. Condition Setting

Convert the network structure of the pores into a file in CAS format and import it into FLUENT. As the units in AVIZO and FLUENT software are different, the grid units need to be unified. Check the quality of the grid to ensure that there are no negative volumes. Set boundary conditions for walls and entrances. This paper mainly considers the effect of different paths and pressure gradient changes on the distribution of pore fissure seepage and flow rate changes, so the simplified model ignores the compressibility of water and the role of gas, does not consider the erosion of water on the rock boundary during seepage and the fracturing effect, measured after the seepage is stable to ignore the error of surface tension. In setting the boundary conditions, the model is divided into three parts: pressurized water, porous media structure, and atmosphere, where the atmospheric pressure is not considered to be influenced by the stratigraphic structure, the pore structure is represented as an airfield, and the pressurized water is set to be pressure driven, essentially a water-driven gas flow simulation. A gravity field of 9.8 m/s^2 was also set in the

y-negative direction, and simulations of seepage under different pressure conditions were carried out in the z-positive and negative directions of the model, respectively, to study the seepage characteristics of the fissure model.

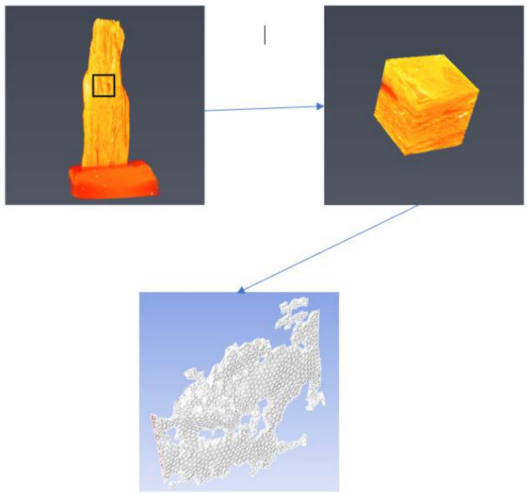

Figure 2. CT scan preprocessing.

3.2. Solver Model Selection

The rough structure of the fracture surface leads to non-Darcy flow, and the exact solution must be obtained by solving the N-S equation [28–30]. When the pore structure of the seepage medium is not considered, the seepage model is commonly used, and the method of studying fluid dynamics is introduced to the entire seepage area. The controlling equations for general incompressible flow have the continuity equation and the N-S component, namely:

$$\frac{\partial u}{\partial t} + u \cdot \nabla\, u = -\frac{1}{\rho}\nabla p + v\nabla^2 u + f \tag{1}$$

$$\nabla \cdot \mathrm{u} = 0 \tag{2}$$

The first of these formulas is the N-S equation, and the second is an incidental formula for incompressible fluids. Where: u is the average velocity of the micro-element section u = nu'; t is the time; ρ is the fluid density; p is the permeation pressure; f is the force per unit mass, and v is the kinematic viscosity coefficient of the fluid.

$$\mathrm{S} = \mathrm{gJ} \tag{3}$$

Substitution of Darcy's theorem:

$$\mathrm{v} = -\mathrm{kJ} \tag{4}$$

$$\mathrm{S} = -\mathrm{g}\frac{v}{k} \tag{5}$$

where: S is the resistance to seepage per unit mass, J is the infiltration ratio, g is the acceleration of gravity.

Because the flow of fluid media within the pores of porous media is predominantly turbulent, simulations are carried out using the standard k-ε model. The advantages of the standard k-ε model are its wide applicability, its low cost, and the high accuracy it can achieve.

3.3. Experimental Design of Seepage Simulation

The control of variables in this experiment mainly lies in the condition setting of the entrance boundary and the selection of different paths. Since the sample fissures are laminar in distribution and there are no obvious through-hole fissures between the fissures, the entrance is set to a certain cross-section of the fissures, and it is also possible to compare the difference of seepage development in different scale fissures by selecting different fissures under the premise of ensuring seepage development. Other factors affecting the effect of seepage include fracture density, connectivity, and tortuosity, which are considered quantitative when the model is determined, and only two variables, pressure gradient, and different fractures, are considered in the experiments of this paper for their effect on the seepage characteristics. The initial pressure at the entrance boundary was divided into several stages, each through a different fissure channel, to see the effect of the two variables in the simulation results on the seepage of the specimen. The DPM model in FLUENT is applied to inject particles and, after post-processing, to observe the trajectory of the particles to see the changes in the flow field and to study the particle flow pattern.

3.4. Seepage Simulation Results and Analysis

The single-fracture structure model of the fault filling was established by means of region selection, the seepage simulation was carried out, and the pressure cloud map and velocity vector diagram at the initial pressure of 0.1 MPa, 0.5 MPa, 1 MPa, 3 MPa, 5 MPa, and 10 MPa at different entrances in the z forward direction and z negative direction were obtained respectively (as shown in Figures 3–6), and the seepage characteristics of the pores of the fault filling and the loss law of the matrix in the skeleton were analyzed.

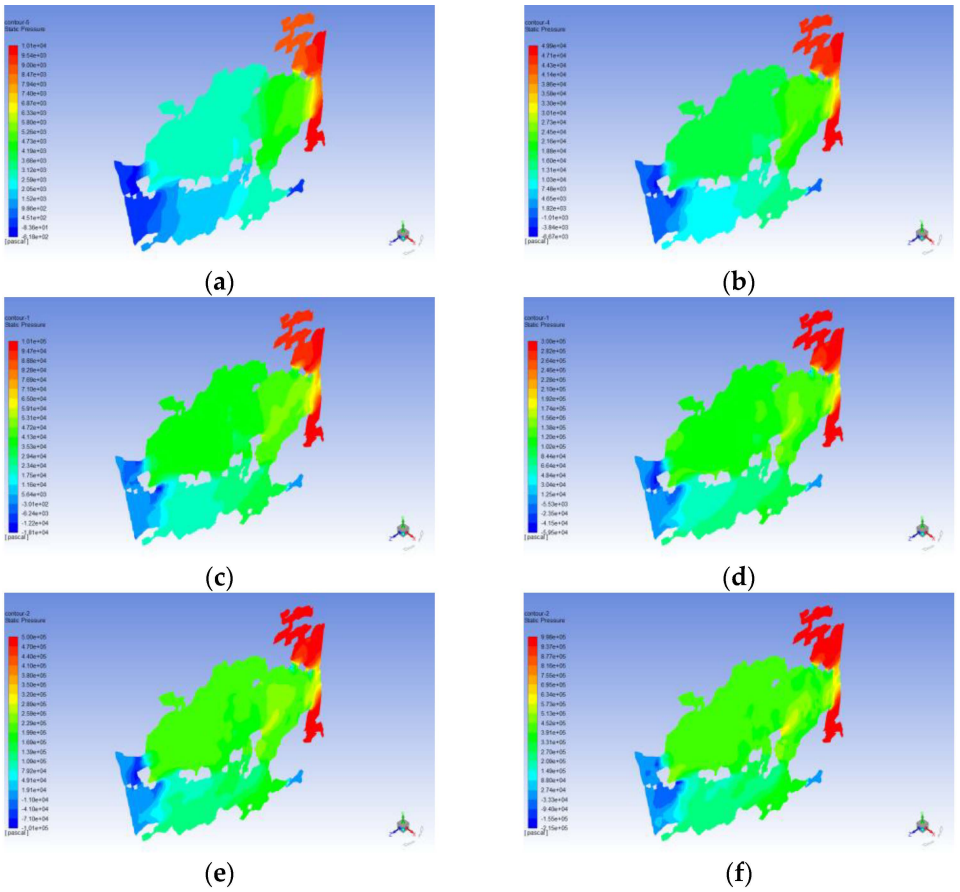

Figure 3. z forward inlet pressure cloud map: (**a**) 0.1 Mpa pressure cloud map. (**b**) 0.5 Mpa pressure cloud map. (**c**) 1 Mpa pressure cloud map. (**d**) 3 Mpa pressure cloud map. (**e**) 5 Mpa pressure cloud map. (**f**) 10 Mpa pressure cloud map.

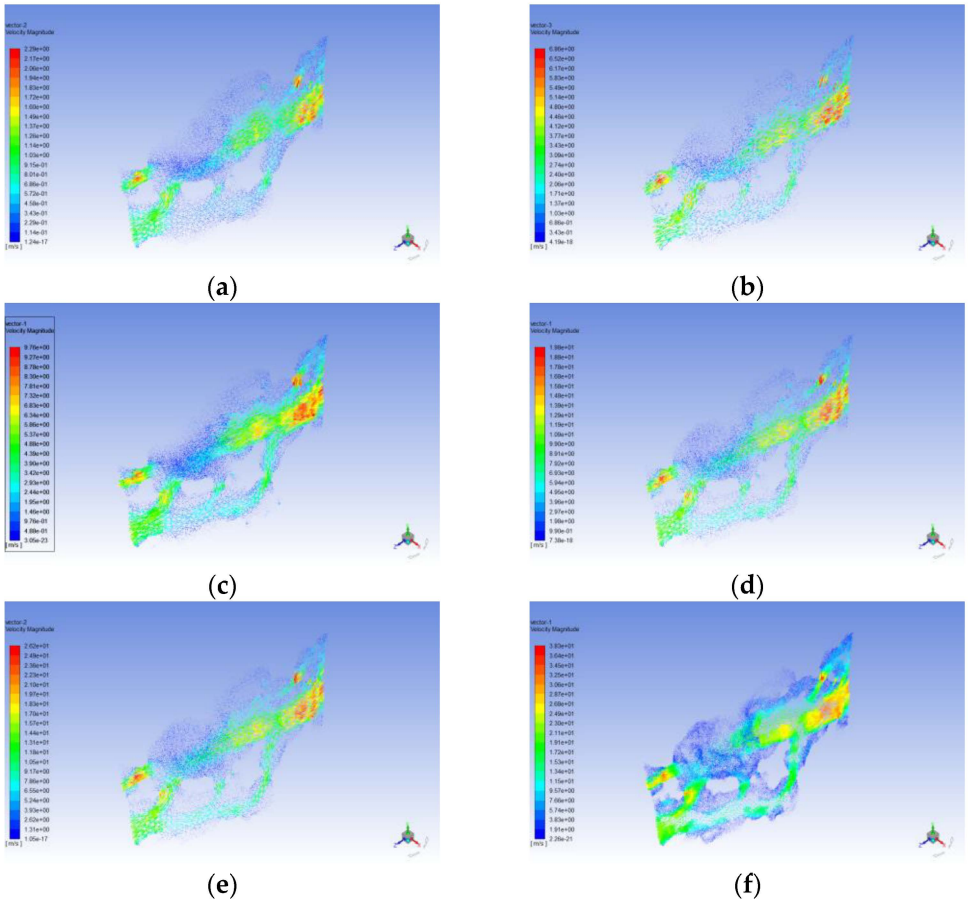

Figure 4. z forward inlet velocity vector diagram:(**a**) 0.1 Mpa speed vector. (**b**) 0.5 Mpa speed vector. (**c**) 1 Mpa speed vector. (**d**) 3 Mpa speed vector. (**e**) 5 Mpa speed vector. (**f**) 10 Mpa speed vector illustration.

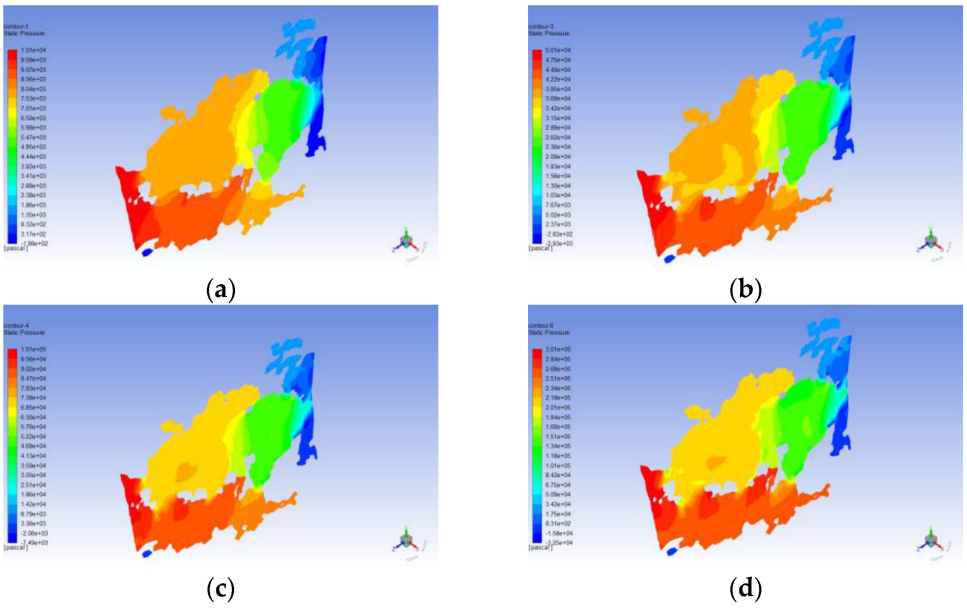

Figure 5. *Cont.*

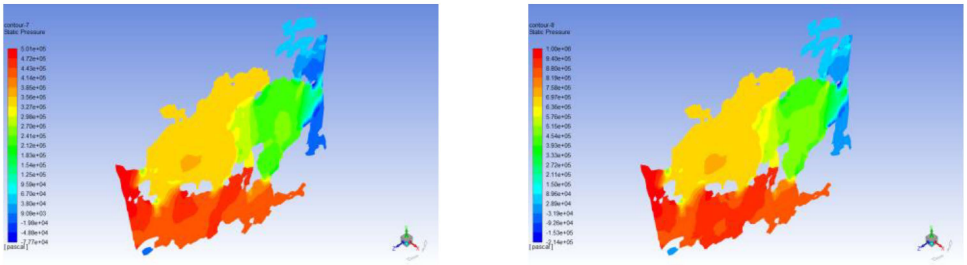

(**e**) (**f**)

Figure 5. z negative inlet pressure cloud map: (**a**) 0.1 Mpa pressure cloud map. (**b**) 0.5 Mpa pressure cloud map. (**c**) 1 Mpa pressure cloud map. (**d**) 3 Mpa pressure cloud map. (**e**) 5 Mpa pressure cloud map. (**f**) 10 Mpa pressure cloud map.

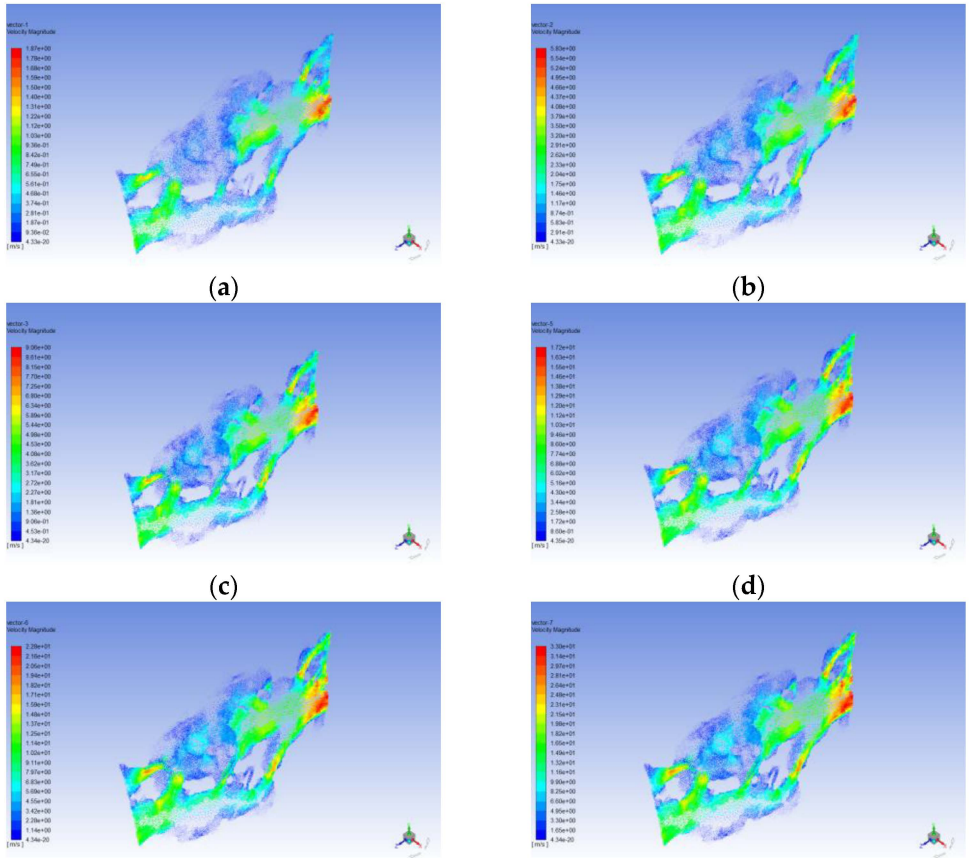

(**a**) (**b**)

(**c**) (**d**)

(**e**) (**f**)

Figure 6. z negative inlet velocity vector diagram:(**a**) 0.1 Mpa speed vector. (**b**) 0.5 Mpa speed vector. (**c**) 1 Mpa speed vector. (**d**) 3 Mpa speed vector. (**e**) 5 Mpa speed vector. (**f**) 10 Mpa speed vector.

The simulation results show that under the same pressure conditions, the seepage of water in different directions of the channel is not exactly the same, which is due to the different pore structure, permeability coefficient, and tortuosity inside the fill. For the pressure distribution, there is a gradual decrease in the direction of water seepage, with pressure changes decreasing before increasing when the pore channels become abruptly large and relatively small pressure changes in areas where the channels change relatively gently. There is no significant change in water seepage in the same direction under different pressure conditions, but as the pressure continues to increase, the rate of water seepage increases.

From Figures 3 and 5, it can be seen that the overall pressure distribution gradually decreases along the direction of water seepage while the velocity increases, which is due to the conversion of fluid pressure potential energy into kinetic energy in the back section of the model and the larger total energy loss due to wall friction and backflow factors.

From Figures 4 and 6, it can be seen that the seepage is divided into three regions: laminar, transitional, and turbulent flow. The flow velocity in the laminar region is low, the viscous force is dominant, and Darcy's law applies. The flow velocity in the transition zone increases, the viscous force becomes smaller, the inertial force increases, and the flow becomes nonlinear laminar flow, and Darcy's law does not apply. Turbulent zone flow velocity is higher, inertial forces dominate, and Darcy's law does not apply. Nonlinear seepage occurs when the seepage velocity is too large or too small. When the seepage velocity is too large, it is the inertial force that dominates and cannot be ignored, while when it is too small, the reason is that the adsorption and hydration membranes affect the linear relationship of seepage, which have different mechanisms and different descriptions, but both cause nonlinear seepage. In multi-phase seepage, the fluid interaction in the porous medium complicates the seepage conditions.

It can be seen from Figures 4–7 that under different pressure conditions, the seepage of water in the same direction does not change significantly, and with the gradual increase in pressure, the seepage speed of water also increases; When the initial pressure increases from 1 MPa to 3 MPa, the maximum velocity increases from 9.7 m/s to 19.8 m/s along the z-positive direction and from 9.1 m/s to 17.2 m/s along the z-negative direction; when the pressure increases from 3 MPa to 5 MPa, the maximum velocity increases from 19.8 m/s to 26.2 m/s in the z-positive direction and from 17.2 m/s to 22.7 m/s. It can be seen that as the initial pressure increases, the water seepage rate eventually plateaus. From Figures 4 and 6, it is obtained that the water seepage in different directions is different under the same pressure conditions, but the overall velocity tends to increase, then decrease, and then increase. This is due to the different tortuosity and permeability coefficients of the microscopic pore structure itself.

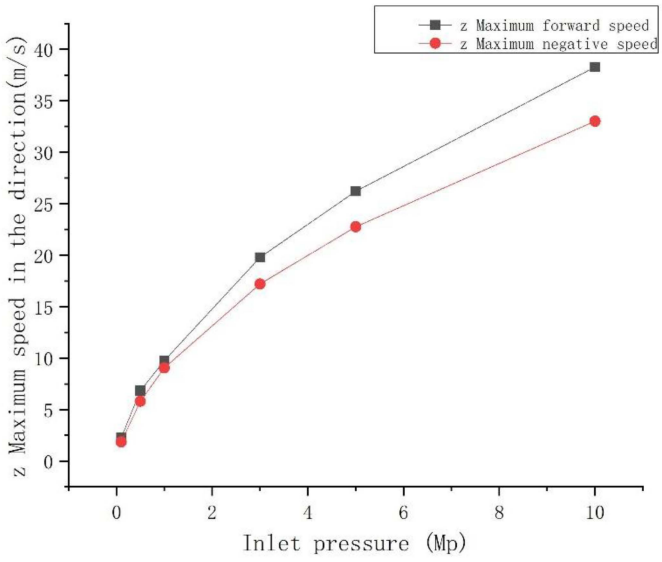

Figure 7. Velocity change diagram under different inlet pressure conditions.

In order to further study the characteristics of water seepage under different fissure model channels and analyze the seepage law, another fissure was selected for simulation, and the pressure cloud and velocity vector diagrams of the model at an initial pressure of 3 MPa were obtained, as shown in Figure 8.

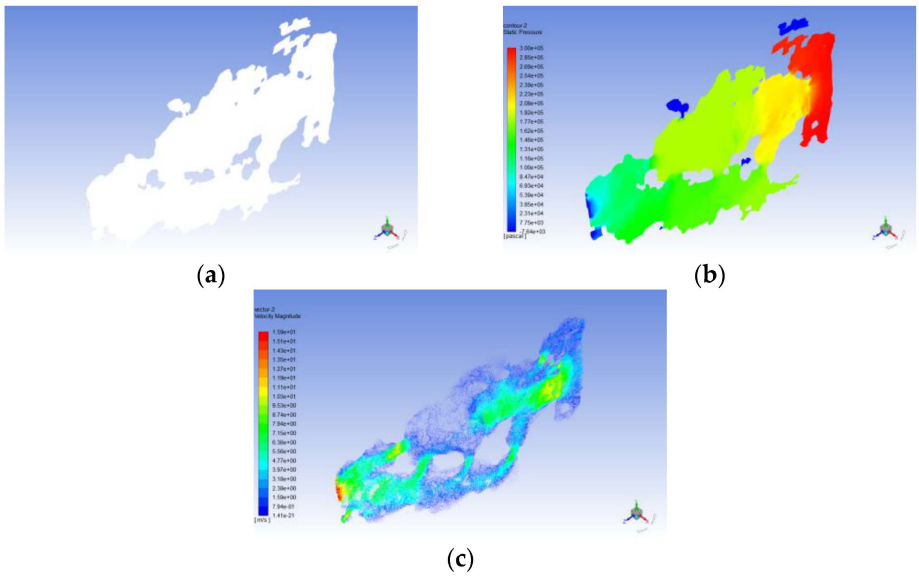

Figure 8. The 3 Mp pressure cloud and speed vector illustration: (**a**) fracture mesh model. (**b**) pressure cloud map. (**c**) speed vector illustration.

From Figures 3, 4 and 8, it can be seen that under the same pressure conditions, the seepage of different fracture models is approximately the same, and for the pressure distribution, different fracture models are gradually decreasing along the direction of water seepage. For the velocity distribution, the seepage flow as a whole tends to increase, then decrease, then increase again. When the pore space suddenly increases, the seepage velocity will decrease; when the pore channel suddenly decreases, the seepage velocity will increase.

In order to visually observe the matrix loss and skeletal seepage routes within the pore space, the DPM modeling method in FLUENT software was used to set the particles to be injected from the entrance surface and set the boundary to reflective particle type, and then the particles were tracked to show the seepage trajectory of the particles within the pore space in a more intuitive way, and the changes in the flow field could be seen through the particle trajectory in the post-processing. This is shown in Figure 9.

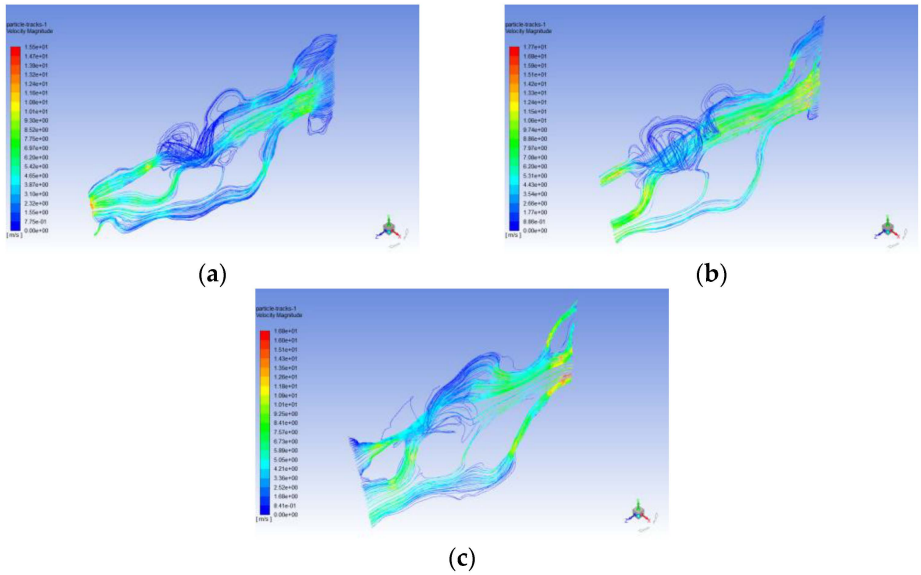

Figure 9. The 3 Mp pressure cloud and speed vector illustration: (**a**) fracture grid motion trajectory. (**b**) z forward motion trajectory diagram. (**c**) z negative motion trajectory diagram.

From Figure 9, it can be found that the particle motion trajectory is in the same direction as the water seepage. From Figure 9a, it can be seen that when the pore channel suddenly increases, the particle motion will generate vortices, and when the pore channel suddenly decreases, the motion velocity will increase. Although there are slight differences in the trajectories of the particles, the overall seepage is more or less the same, with the seepage velocity first increasing, then decreasing, and then increasing again.

4. Discussion

In the change of fault geological structure, the size, shape, and distribution of the fault-fill skeletal pore fractures differ greatly from those of sedimentary and magmatic rocks due to stress and metamorphism and are related to their mineral composition and degree of metamorphism, which inevitably has an impact on the general evaluation of fault-fill skeletal pore fractures. Compared with mudstone, kinetic metamorphic schist has more stable structural characteristics under water-rock action and contains more fractures along the grain direction, making it easy to obtain fracture models. Therefore, in the simulation experiments, CT scans and 3D model reconstructions were carried out using a sample of dynamically metamorphosed schist in the skeleton of the fill. The numerical simulation of seepage flow is used to analyze the evolutionary patterns affecting the seepage characteristics of the fractures from different directional channels and under different initial pressure conditions.

The seepage characteristics of the fracture skeleton can be controlled or influenced by a variety of factors. The tortuosity of the fractures can lead to differences in flow rates in the seepage field, which inevitably affect the evolution of the seepage characteristics. Differences in the pore structure within the fill are also inherent conditions affecting the evolution of the seepage characteristics. Typically, seepage characterization studies rarely involve aspects of differently oriented channels, so this simulated experimental study presents the seepage characteristics of channels in opposite directions in the same fissure.

As shown in Figures 3–7, the pressure and velocity distributions for the z-positive and z-negative inlet models show that the channel water seepage characteristics are similar in different directions. The overall pressure distribution pattern is similar in both positive and negative directions, with the pressure gradually decreasing along the direction of water seepage and the pressure change showing a trend of first decreasing and then increasing when the fissure channel suddenly becomes larger. The overall trend of velocity change in the positive and negative directions is to decrease and then increase. There is no significant change in the seepage of water in the same direction under different pressure conditions. As the pressure continues to increase, the seepage rate of water continues to increase but eventually tends to a steady state. As shown in Figures 3, 4 and 8, the seepage is approximately the same for the different fracture models under the same pressure conditions.

5. Conclusions

(1) A 3D skeleton model containing the fracture structure was constructed based on CT images of the coal mine fault fill. On this basis, the fracture structure data of the fault fill were obtained, and the seepage simulation of the fracture structure with control variables was combined with FLUENT. The seepage characteristics of the fill were analyzed, and data on the pressure and flow velocity distribution during seepage were obtained for the fracture structure model of the fill.

(2) In the microscopic case of filling fractures, seepage under different pressure conditions is approximately the same, and the rate increases continuously with increasing pressure. Under the same pressure conditions, the water seepage of fracture channels in different directions is not exactly the same, which is caused by the different microstructure of pores. For the pressure distribution, gradually decreases along the direction of water seepage, and for the speed distribution, it shows the law of changing from large to small and then increasing.

(3) By tracing the particle trajectory, it is found that vortices occur when the fissure channel suddenly increases, and the velocity of motion increases when the pore channel suddenly becomes smaller. Although there are subtle differences in particle trajectories, the overall seepage pattern is roughly the same, with the seepage velocity first increasing, then decreasing, and then increasing again.

(4) The seepage of the rock fracture structure in the fault fill is consistent with the characteristics of groundwater seepage, which is characterized by a decrease in pressure and an increase in flow rate when the fracture opening decreases due to the conversion of fluid pressure potential energy into kinetic energy in the back section of the model, and a larger total energy loss due to wall friction and backflow.

Author Contributions: S.W.: software, investigation, data curation, writing review. W.S.: Conceptualization, data curation, methodology, writing—original draft. F.D.: supervision, software, funding acquisition, validation. Y.X.: writing-review and editing, investigation. All authors have read and agreed to the published version of the manuscript.

Funding: This study was financially supported by the National Natural Science Foundation of China (No.51974172, 52274131), Shandong Higher Education Youth Innovation and Technology Program (2020KJH001), State Key Laboratory of Coal Mining and Clean Utilization (2021-CMCU-KF017).

Institutional Review Board Statement: Not applicable.

Informed Consent Statement: Not applicable.

Data Availability Statement: Not applicable.

Acknowledgments: Special thanks to the Key Laboratory of Intelligent Control and Green Mining of Mining Formations, Shandong University of Science and Technology, for providing the support of cross-scale core scanning experimental equipment.

Conflicts of Interest: The authors declare no conflict of interest.

References

1. Zhao, J.; Bo, L.; Chen, J.; Ning, J. Mechanism of Seepage-Stress Fault Water Inrush and Grouting Seal. *Arab. J. Geosci.* **2020**, *13*, 4259–4279. [CrossRef]
2. Qian, Z.; Huang, Z.; Song, J. A case study of water inrush incident through fault zone in China and the corresponding treatment measures. *Arab. J. Geosci.* **2018**, *11*, 381. [CrossRef]
3. Zheng, Z.; Yu, F.; Hao, W.; Jia, R.; Yu, L. The Non-Darcy Characteristics of Fault Water Inrush in Karst Tunnel Based on Flow State Conversion Theory. *Therm. Sci.* **2021**, *25*, 4415–4421.
4. Wang, P.; Xu, J.; Li, C. Similar Simulation Test Study on Permeability Evolution Mechanism of Fault Sliding Fracture Zone. *Arab. J. Geosci.* **2022**, *15*, 548. [CrossRef]
5. Shao, J.; Zhou, F.; Sun, W. Evolution Model of Seepage Characteristics in the Process of Water Inrush in Faults. *Geofluids* **2019**, *2019*, 4926768. [CrossRef]
6. Zhu, Z.; Niu, Z.; Que, X.; Liu, C.; He, Y.; Xie, X. Study on Permeability Characteristics of Rocks with Filling Fractures Under Coupled Stress and Seepage Fields. *Water* **2020**, *12*, 2782. [CrossRef]
7. Shao, J.; Zhang, Q.; Wu, X.; Lei, Y.; Wu, X.; Wang, Z. Investigation on the Water Flow Evolution in a Filled Fracture under Seepage-Induced Erosion. *Water* **2020**, *12*, 3188. [CrossRef]
8. Xue, S.; Yuan, L.; Wang, Y.; Xie, J. Numerical Analyses of the Major Parameters Affecting the Initiation of Outbursts of Coal and Gas. *Rock Mech. Rock Eng.* **2014**, *47*, 1505–1510. [CrossRef]
9. Hao, Z.; Sun, G.; Zhang, G. Mechanism and Inducing Factors of Rockburst Events of Roadways Under Ultrathick Strata. *Front. Earth. Sc-Switz.* **2022**, *10*, 860929. [CrossRef]
10. Zhang, Q.; Jiang, Q.; Zhang, X.; Wang, D. Model test on development characteristics and displacement variation of water and mud inrush on tunnel in fault fracture zone. *Nat. Hazards.* **2019**, *99*, 467–492. [CrossRef]
11. Li, S.; Bu, L.; Shi, S.; Li, L.; Zhou, Z. Prediction for Water Inrush Disaster Source and CFD-Based Design of Evacuation Routes in Karst Tunnel. *Int. J. Geomech.* **2022**, *22*, 05022001. [CrossRef]
12. Salzer, M.; Prill, T.; Spettl, A. Quantitative comparison of segmentation algorithms for FIB-SEM images of porous media. *J. Microsc. Oxford* **2014**, *257*, 23–30. [CrossRef] [PubMed]
13. Wu, Y.; Li, Y.Z.; Qiao, W.G.; Fan, Z.W.; Zhang, S.; Chen, K.; Zhang, L. Water Seepage in Rocks at Micro-Scale. *Water* **2022**, *14*, 2827. [CrossRef]

14. Ju, Y.; Xi, C.; Zheng, J.; Gong, W.; Wu, J.; Wang, S.; Mao, L. Study on three-dimensional immiscible water–Oil two-phase displacement and trapping in deformed pore structures subjected to varying geostress via in situ computed tomography scanning and additively printed models. *Int. J. Eng. Sci.* **2022**, *171*, 103615. [CrossRef]
15. Wang, M.; Yang, S.; Li, J.; Zheng, Z.; Wen, J.; Ma, Q.; Wang, Q.; Chen, H. Cold water-flooding in a heterogeneous high-pour-point oil reservoir using computerized tomography scanning: Characteristics of flow channel and trapped oil distribution. *J. Pet. Sci. Eng.* **2021**, *202*, 108594. [CrossRef]
16. Dong, C.; Nemkumar, B.; Wang, Q.; Sun, W. Investigation on porosity of partly carbonated paste specimens blended with fly ash through dual CT scans. *Constr. Build. Mater.* **2019**, *196*, 692–702.
17. Yang, Y.; Yang, H.; Tao, L.; Yao, J.; Wang, W.; Zhang, K. Microscopic Determination of Remaining Oil Distribution in Sandstones with Different Permeability Scales Using Computed Tomography Scanning. *J. Energy Resour. Technol.* **2019**, *141*, 092903. [CrossRef]
18. Zhou, G.; Zhang, Q.; Bai, R.; Ni, G. Characterization of Coal Micro-Pore Structure and Simulation on the Seepage Rules of Low-Pressure Water Based on CT Scanning Data. *Minerals* **2016**, *6*, 78. [CrossRef]
19. Choi, C.; Lee, Y.; Song, J. Equivalent Pore Channel Model for Fluid Flow in Rock Based on Microscale X-ray CT Imaging. *Materials* **2020**, *13*, 2619. [CrossRef]
20. Qiu, L.; Zhou, G.; Zhang, W.; Han, W. Simulations on the micro-seepage rules of gas and water based on micro-CT/CFD and the related contrastive analysis. *Arab. J. Geosci.* **2019**, *12*, 549. [CrossRef]
21. Liu, W.; Wang, G.; Han, D.; Xu, H.; Chu, X. Accurate characterization of coal pore and fissure structure based on CT 3D reconstruction and NMR. *J. Nat. Gas. Sci. Eng.* **2021**, *96*, 104242. [CrossRef]
22. Zhao, L.; Ni, G.; Wang, Y.; Jiang, H.; Wen, Y.; Dou, H.; Jing, M. Semi-homogeneous model of coal based on 3D reconstruction of CT images and its seepage-deformation characteristics. *Energy* **2022**, *259*, 125044. [CrossRef]
23. Liu, J.; Wang, Y.; Song, R. A Pore Scale Flow Simulation of Reconstructed Model Based on the Micro Seepage Experiment. *Geofluids* **2017**, *2017*, 7459346. [CrossRef]
24. Wang, G.; Jiang, C.; Shen, J.; Han, D.; Qin, X. Deformation and water transport behaviors study of heterogenous coal using CT-based 3D simulation. *Int. J. Coal. Geol.* **2019**, *211*, 103204. [CrossRef]
25. Wang, G.; Shen, J.; Liu, S.; Jiang, C.; Qin, X. Three-dimensional modeling and analysis of macro-pore structure of coal using combined X-ray CT imaging and fractal theory. *Int. J. Rock. Mech. Min.* **2019**, *123*, 104082. [CrossRef]
26. Yao, B.; Chen, Z.; Wei, J.; Bai, T.; Liu, S. Predicting Erosion-Induced Water Inrush of Karst Collapse Pillars Using Inverse Velocity Theory. *Geofluids* **2018**, *2018*, 2090584. [CrossRef]
27. Li, L.; Hu, J.; Li, S.; Qin, C.; Liu, H.; Chen, D.; Wang, J. Development of a Novel Triaxial Rock Testing Method Based on Biaxial Test Apparatus and Its Application. *Rock. Mech. Rock. Eng.* **2021**, *54*, 1597–1607. [CrossRef]
28. Wang, Y.; Sun, S.; Yu, B. On Full-Tensor Permeabilities of Porous Media from Numerical Solutions of the Navier-Stokes Equation. *Adv. Mech. Eng.* **2013**, *5*, 137086. [CrossRef]
29. Shi, R.; Lin, J.; Yang, H. Distribution of Nanoparticles in a Turbulent Taylor–Couette Flow Considering Particle Coagulation and Breakage. *Processes* **2021**, *9*, 1789. [CrossRef]
30. Zou, L.; Jing, L.; Cvetkovic, V. Modeling of flow and mixing in 3D rough-walled rock fracture intersections. *Adv. Water Resour.* **2017**, *107*, 1–9. [CrossRef]